Optical spectroscopy of Pr^{3+} in $M^{+}Bi(XO_4)_2$, M^{+} = Li or Na and X = W or Mo, locally disordered single crystals

2004 J. Phys.: Condens. Matter 16 2139

(http://iopscience.iop.org/0953-8984/16/12/023)

INSTITUTE OF PHYSICS PUBLISHING JOURNAL OF PHYSICS: CONDENSED MATTER

J. Phys.: Condens. Matter **16** (2004) 2139–2160 PII: S0953-8984(04)72938-0

Optical spectroscopy of Pr^{3+} in $M^+Bi(XO_4)_2$, M^+ = Li or Na and X = W or Mo, locally disordered single crystals

A Méndez-Blas[1], M Rico[1], V Volkov[1], C Cascales[1], C Zaldo[1,5], C Coya[2], A Kling[3,4] and L C Alves[3,4]

[1] Instituto de Ciencia de Materiales de Madrid, Consejo Superior de Investigaciones Científicas, Cantoblanco, 28049 Madrid, Spain
[2] Escuela Superior de Ciencias Experimentales y Tecnología, Universidad Rey Juan Carlos, Móstoles, 28933 Madrid, Spain
[3] Instituto Tecnológico e Nuclear, Estrada Nacional No 10, 2686-953 Sacavém, Portugal
[4] Centro de Física Nuclear da Universidade de Lisboa, Avenida Profesor Gama Pinto 2, 1649-003 Lisboa, Portugal

E-mail: cezaldo@icmm.csic.es

Received 2 December 2003
Published 12 March 2004
Online at stacks.iop.org/JPhysCM/16/2139 (DOI: 10.1088/0953-8984/16/12/023)

Abstract

$NaBi(WO_4)_2$ (NBW), $NaBi(MoO_4)_2$ (NBMo) and $LiBi(MoO_4)_2$ (LBMo) single crystals grown by the Czochralski technique have been doped up to a praseodymium concentration of $[Pr] \approx 1 \times 10^{20}$ cm^{-3} in the crystal. 10 K polarized optical absorption and photoluminescence measurements have been used to determine the energy position of 32, 39 and 36 Pr^{3+} Stark levels in NBW, NBMo and LBMo crystals, respectively. These energy levels were labelled with the appropriate irreducible representations corresponding to a C_2 local symmetry of an average optical centre. Single-electron Hamiltonians including free-ion and crystal field interactions have been used in the fitting of experimental energy levels and in the simulation of the full sequence of the $4f^2$ Pr^{3+} configuration. 300 K absorption spectra of different $^{2S+1}L_J Pr^{3+}$ multiplets were determined and used in the context of the Judd–Ofelt theory and for the calculation of the $^1D_2$-related emission cross sections of this average Pr^{3+} centre. Non-radiative electron relaxation from the $^3P_0$ level feeds the $^1D_2$ multiplet. This latter level efficiently decays radiatively to the ground $^3H_4$ multiplet but still there is a significant rate of radiative decay to the $^1D_2 \rightarrow {}^3F_3$ praseodymium laser channel. For $[Pr] \geqslant 2 \times 10^{19}$ cm^{-3}, non-radiative electric dipole–dipole Pr pair energy transfer limits the radiative yield.

[5] Author to whom any correspondence should be addressed.

1. Introduction

$NaBi(WO_4)_2$ (NBW) and $NaBi(MoO_4)_2$ (NBMo) single crystals are currently of interest since they exhibit large values of the χ^3 non-linear constant characterizing the stimulated laser Raman shifting phenomena [1]. The use of $LiBi(MoO_4)_2$ (LBMo) is less developed but it has similar Raman properties than the former two crystals [2].

These crystals have crystalline structure related to the tetragonal scheelite-type of $CaWO_4$. The substitution for Ca^{2+} of a combination of monovalent and trivalent cations gives rise to a large number of double tungstate and double molybdate compounds [3]. Although most of these compounds have a high temperature tetragonal phase, some of them (those based on K, Rb and Cs) undergo upon cooling a phase transition to lower symmetry structures. By contrast, the Na^+–Bi^{3+}–W/Mo and Li^+–Bi^{3+}–Mo combinations remain in the tetragonal phase. In these latter cases a random distribution of monovalent and trivalent cations in non-equivalent lattice sites occurs and the bands associated with optical transitions of trivalent rare earth (RE) impurities replacing Bi^{3+} are broad. This spectral broadening can be useful in laser systems pumped by semiconductor diodes, since the spectral emission bandwidths of common diodes are several nanometres and therefore a more efficient absorption takes place in broadened bands.

In the present work we analyse the fluorescence properties of Pr^{3+} in NBW, NBMo and LBMo disordered crystals. Attention is paid to the Pr^{3+} $^1D_2$ manifold since $^1D_2 \rightarrow {}^3F_4$ lasing has been observed for $\lambda \approx 1.06$–1.07 μm [4] and $^1D_2 \rightarrow {}^3F_3$ lasing at $\lambda \approx 1.02$ μm [5]. To a lesser extent, attention is also paid to the $^1G_4$ manifold, sometimes considered as responsible for stimulated emission at $\lambda \approx 1.3$ μm ($^1G_4 \rightarrow {}^3H_5$ transition) [6].

Using low temperature (10 K) polarized spectroscopic techniques and crystal field modelling we have determined Pr^{3+} energy levels from $^3H_4$ up to $^3P_2$ and confirmed the large bandwidth of the spectral bands. Radiative and non-radiative processes of Pr^{3+} have been studied.

2. Crystal structure and growth procedures

An overview of the crystal chemistry and growth of NBW and NBMo has been given recently [7]. According to the available information, NBW and NBMo hosts are isostructural and belong to the non-centrosymmetric space group $I\bar{4}$ (No 82), $Z = 2$ [8, 9]. LBMo can also be indexed in the same space group with $a = 5.2200(11)$ Å and $c = 11.482(4)$ Å [10]. Na^+/Li^+ and Bi^{3+} cations share two non-equivalent lattice sites, 2d and 2b, both with local symmetry S_4, but with different occupancy factors, namely 60% Bi + 40% Na and 40% Bi + 60% Na for 2d and 2b sites, respectively, in NBW [8] and 55% Bi + 45% Na and 45% Bi + 55% Na for 2d and 2b sites in NBMo [9] and LBMo [10]. The optical axis for RE in 2d and 2b sites is parallel to the crystallographic c-axis.

Due to their congruent melting, single crystals of NBW, NBMo and LBMo can be pulled by the Czochralski technique. Pr doped single crystals with optical quality were obtained by reacting the host compounds with 99.9% Pr_2O_3 from CERAC Inc. for ~100 h at 860 °C for tungstates and 785 °C for molybdates. The products were melted in Pt crucibles and crystals were pulled at the following rates: 0.8–4 mm h^{-1} for NBW, 1.3–2.3 mm h^{-1} for NBMo and 1.7–1.9 mm h^{-1} for LBMo. More details of the growth procedures have been given previously [7, 11].

Pr concentrations in the crystal have been measured by total reflection x-ray fluorescence (TRXF), proton induced x-ray emission (PIXE) and electron probe microanalysis (EPMA) techniques. Our Pr concentrations are close to the resolution limits of the above three techniques; therefore the concentration measurements may have an uncertainty of about 40% of

the absolute value reported. For praseodymium concentrations of up to $[Pr] = 0.8 \times 10^{20}\,cm^{-3}$ (or $\sim$1.0 mol%) we can still obtain samples some cubic centimetres in size, free of macroscopic defects and with optical quality for spectroscopic measurements.

3. Experimental techniques

Ground state optical absorption (GSA) was recorded in a Varian spectrophotometer, model CARY-5E. Photoluminescence (PL) was excited with the Rhodamine R-6G ($\lambda \approx 591$ nm) or Curamin-480 ($\lambda \approx 485$ nm) emissions of a dye laser (LSI, model DUO-220); the praseodymium emission was dispersed with a Spex 340E spectrometer using 1200 or 600 l mm^{-1} gratings. The light was detected with a cooled R928 Hamamatsu photomultiplier ($\lambda = 0.35$–$0.95\ \mu$m) and with a 77 K cooled Ge photodiode ($\lambda = 0.8$–$2.5\ \mu$m). To record the spectral distributions we used a lock-in amplifier while for lifetime measurements the signal was monitored with a 500 MHz Tektronix TDS520 digital oscilloscope. The PL system was spectrally calibrated with an EGG tungsten halogen lamp standard. The Pr^{3+} emission peaking at the overlap region ($\lambda = 0.8$–$0.95\ \mu$m) of the spectral responses of the R928 photomultiplier and the Ge photodiode was used for a relative calibration of the system responsivity when using different grating and detector configurations. These calibrations allow one to determine the experimental emission branching ratios. In the spectroscopic experiments the sample temperature was selected by using a He closed cycle cryostat connected to a suitable temperature controller.

Reduction annealings in vacuum (10^{-3} mbar) were made in a stainless steel tube, dynamically evacuated. The tube is introduced in a conventional furnace and the samples are stored inside the tube in a platinum box to avoid contamination. The annealing temperature was tested with a thermocouple in contact with the Pt box.

4. Experimental results

4.1. Praseodymium valence state

Pr_2O_3 powder stored at room conditions may experience oxidation to the Pr^{4+} state. In some oxides, praseodymium can be incorporated as Pr^{4+}; in particular this happens in oxides with tetravalent cation sites, such as $BaPrO_3$ [12] or ZrO_2-based ones [13], and in those grown under charge compensation conditions, such as YAG:Pr:Mg [14].

In $M^+Bi(XO_4)_2$ crystals the $1M^+$:$1Bi^{3+}$ ratio leads to 2+ average charge (like Ca^{2+} in the scheelite). The substitution of Pr^{4+} for Bi^{3+}, keeping the 2+ average charge for M^+:$(Bi^{3+})_{1-x}$ + $(Pr^{3+,4+})_x$, can be *a priori* envisaged as a charge compensation mechanism involving the enhancement of the M^+:Bi^{3+} ratio. Therefore this possibility must be considered. Pr^{4+} can contribute to the optical absorption with crystal field transitions in the infrared ($\lambda \approx$ 2000–1400 nm) and by 4f $\rightarrow$ 5d interconfiguration transitions in the visible and ultraviolet.

It has been shown that NBMo crystal annealed in vacuum exhibits a reduction process [7]. It is thought that this process may reduce any Pr^{4+} in the sample to Pr^{3+}. Figures 1 and 2 show the optical absorptions of NBMo:Pr and LBMo:Pr crystals respectively for different reduction times. Before reduction the spectra consist of relatively sharp lines typically associated with Pr^{3+} ions. In both hosts, the reduction develops very broad bands overlapping the Pr^{3+} spectrum. The broad bands are due to light absorption in the lattice defects (oxygen vacancies and/or trapped holes) created by the vacuum annealing. The Pr^{3+} absorption close to $\lambda \approx 2000$ nm overlaps little with the broad bands created by reduction; therefore the spectrophotometer linearity is ensured in this spectral region.

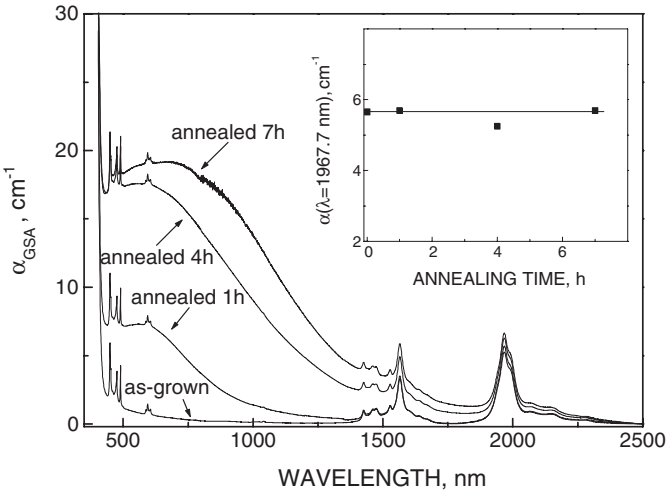

Figure 1. Evolution during 10^{-3} mbar vacuum annealing of the 300 K ground state optical absorption coefficient (α_{GSA}) of NBMo:Pr crystals. The inset shows α at $\lambda = 1967.7$ nm.

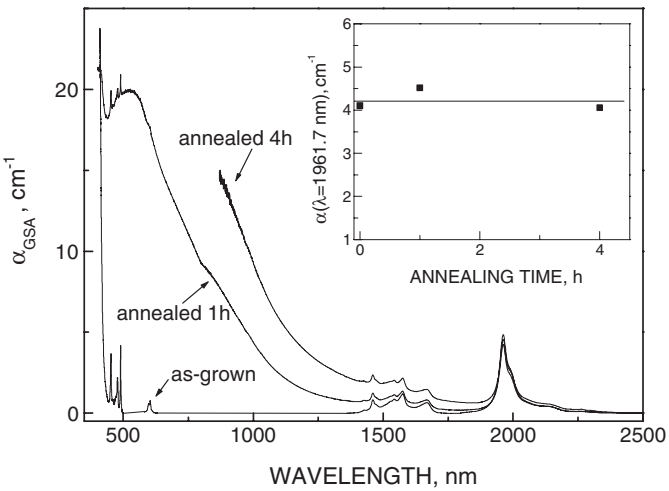

Figure 2. Evolution during 10^{-3} mbar vacuum annealing of the 300 K ground state optical absorption coefficient (α_{GSA}) of LBMo:Pr crystals. The inset shows α at $\lambda = 1961.7$ nm.

The insets of figures 1 and 2 show that the intensities of these Pr^{3+} bands do not increase during the reduction treatment. The very minor changes observed are within the uncertainty of the sample repositioning and background correction procedure. Therefore we conclude that praseodymium incorporates into NBMo and LBMo exclusively as Pr^{3+}. Similar experiments are not possible for NBW since this crystal does not experience reduction upon annealing in vacuum; however, the lack of significant pre-edge absorption and the similarity of the optical spectra with those of molybdate crystals suggest that praseodymium enters primarily as Pr^{3+}.

4.2. Pr^{3+} energy levels

4.2.1. Low temperature ground state absorption and photoluminescence. J-manifolds of the $4f^2$ configuration of Pr^{3+} split into Stark levels by interaction with the lattice crystal field.

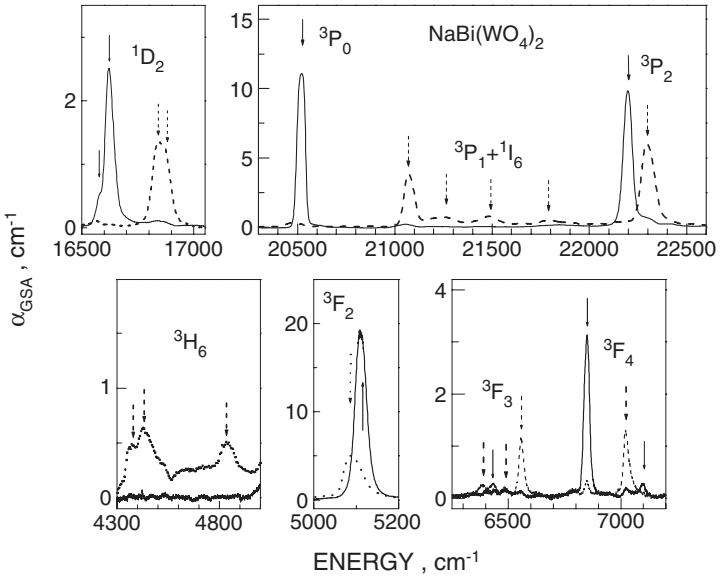

Figure 3. The 10 K polarized ground state optical absorption coefficient, α_{GSA}, of Pr^{3+} in NBW. $[Pr] = 0.24 \times 10^{20}$ cm^{-3}. Continuous curves: π-spectra. Dashed curves: σ-spectra.

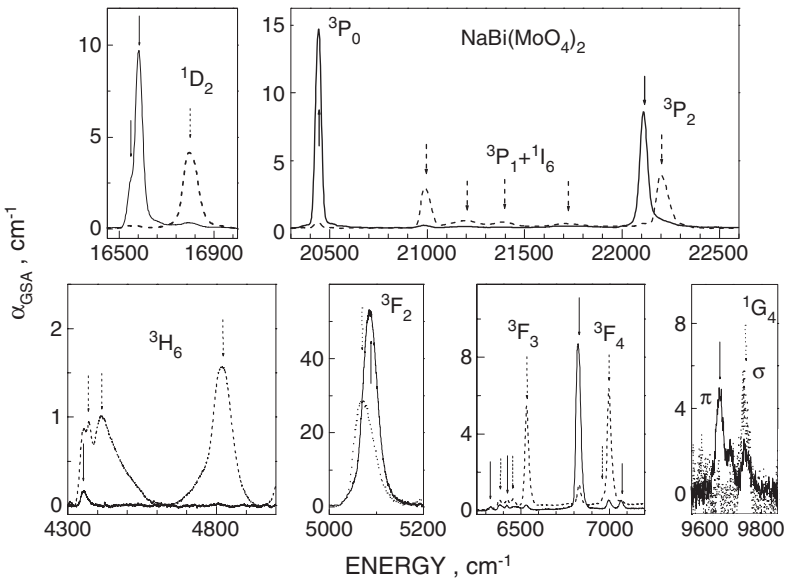

Figure 4. The 10 K polarized ground state optical absorption coefficient, α_{GSA}, of Pr^{3+} in NBMo. $[Pr] = 0.5 \times 10^{20}$ cm^{-3}. Continuous curves: π-spectra. Dashed curves: σ-spectra.

Figures 3 and 4 show the 10 K GSA polarized spectra of Pr^{3+} in $NaBi(XO_4)_2$, X = W or Mo respectively. The spectra of Pr^{3+} in LBMo are very similar to those of NBMo; therefore they are not shown for the sake of brevity. According to the tetragonal character of the lattices, the experimental spectra are labelled as $\sigma(E \perp c, H \parallel c)$ or $\pi(E \parallel c, H \perp c)$. These measurements give the position of the Stark levels from $^3H_6$ up to $^3P_2$ manifolds (except for $^1G_4$ in NBW). No experimental evidence of vibronically assisted transitions [15] was found.

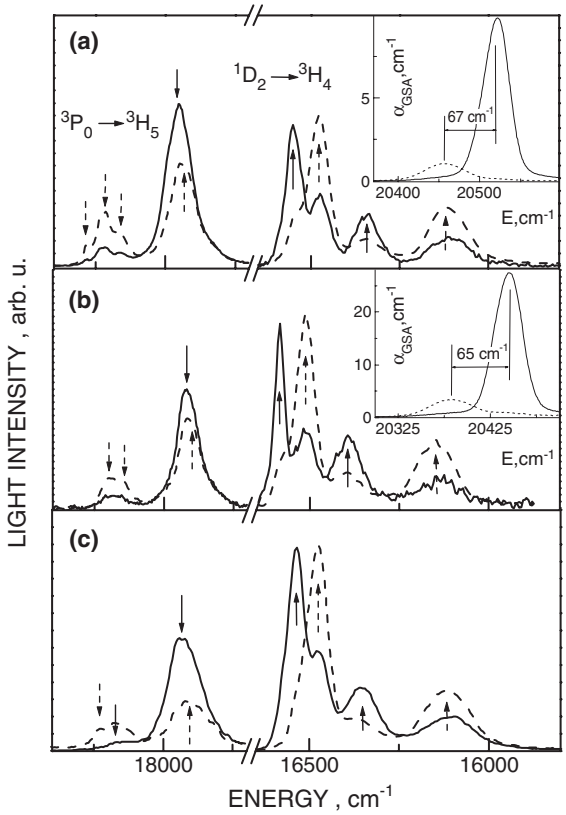

Figure 5. The 10 K polarized Pr^{3+} photoluminescence in (a) NBW, (b) NBMo and (c) LBMo crystals. $^3P_0 \rightarrow {}^3H_5$, $\lambda_{exc} = 488$ nm; $^1D_2 \rightarrow {}^3H_4$, $\lambda_{exc} = 591$ nm. The inset shows the 100 K polarized ground state optical absorption coefficient, α_{GSA}, of the $^3P_0$ multiplet in (a) NBW and (b) NBMo crystals. Continuous curves: π-spectra. Dashed curves: σ-spectra.

The energies of the Stark levels of the ground $^3H_4$ multiplet have been established from the PL of the $^1D_2$ lowest Stark level, while the positions of the $^3H_5$ Stark levels were determined from the PL of the $^3P_0$ singlet; both emissions are shown in figure 5. The energy of the first excited Stark level of the $^3H_4$ multiplet has been further assessed via the thermal behaviour of the GSA; see the insets of figure 5. In summary, 32 Pr^{3+} energy levels in NBW, 39 in NBMo and 36 in LBMo have been determined and are collected in table 1. The low praseodymium concentration and the inhomogeneous broadening that weakens the peak intensities hamper the experimental determination of a larger number of levels.

It is worth noting that the 10 K GSA of the $^3P_0$ multiplet shows a single π-polarized band in the three matrices. The spectral bandwidth of this transition is rather large in all cases, namely $\sim$48 cm^{-1} in NBW, $\sim$35 cm^{-1} in NBMo and $\sim$45 cm^{-1} in LBMo, and the individual optical responses of Pr^{3+} in 2b and 2d crystal sites are not resolved in these GSA spectra or in the $^3P_0$ PL shown in figure 5. In what follows we will consider an average centre to describe the optical properties of Pr^{3+} in the above matrices.

Despite the S_4 local symmetry of the Bi^{3+} in the $I\bar{4}$ space group, it has been shown that the spectroscopic properties of RE^{3+} ions with large ionic radii, such as Nd^{3+}, have to be interpreted under the assumption of a lower short-range symmetry, namely C_2 [16], by contrast to Er^{3+}, with lower ionic radius, which exhibits properties according to the S_4 symmetry [17]. In general, the

Table 1. Energy levels (in cm^{-1}) of Pr^{3+}, observed at 10 K (E_o) and calculated (E_c) in C_2 symmetry for $M^{+}Bi(XO_4)_2$ X = Mo, W crystals. IR indicates the corresponding irreducible representation, $A' \equiv \Gamma_1$ and $A'' \equiv \Gamma_2$. $\|$ indicates the experimental polarization of the absorption bands, i.e. z for π-spectra and x, y for σ-spectra.

			NBW		NBMo		LBMo	
$^{2S+1}L_J$	IR	$\|$	E_o	E_c	E_o	E_c	E_o	E_c
$^3H_4$	A'	z	0	4	0	5	0	0
	A''	x, y	67	66	65	57	62	57
	A''		—	160	—	117	—	125
	A'	z	207	214	192	214	183	203
	A'		—	272	—	259	—	231
	A''	x, y	441	437	438	423	418	415
	A'		—	451	—	434	—	416
	A''		—	512	—	481	—	506
	A'		—	555	—	501	—	503
$^3H_5$	A''	x, y	—	2196	—	2218	2192	2196
	A'		—	2218	—	2211	—	2200
	A'		—	2234	—	2243	—	2245
	A''	x, y	2235	2239	2248	2236	—	2226
	A'	z	—	2269	—	2261	2250	2251
	A''	x, y	2307	2299	2302	2296	—	2263
	A''	x, y	2355	2345	—	2330	—	2299
	A'	z	—	2475	—	2487	2482	2479
	A''	x, y	—	2522	2532	2518	2514	2505
	A'	z	2567	2552	2526	2539	—	2539
	A''	x, y	2572	2576	—	2552	—	2555
$^3H_6$	A'		—	4191	—	4254	—	4229
	A''		—	4230	—	4295	—	4271
	A'		—	4301	—	4318	—	4293
	A''		—	4310	—	4317	—	4334
	A'	z	—	4334	4355	4355	4350	4346
	A''	x, y	4379	4383	4371	4367	4353	4348
	A'		—	4393	—	4424	—	4383
	A''	x, y	4429	4448	4415	4536	4415	4435
	A'		—	4511	—	4514	—	4474
	A''		—	4719	—	4744	—	4742
	A'		—	4745	—	4756	—	4748
	A'		—	4829	—	4807	4803	4809
	A''	x, y	4836	4829	4818	4806	4834	4818
$^3F_2$	A'		—	5079	—	5057	—	5053
	A''	x, y	5088	5091	5069	5071	5066	5050
	A''		—	5111	—	5077	—	5070
	A'	z	5111	5127	5085	5090	5085	5085
	A'		—	5207	—	5165	—	5174
$^3F_3$	A''		—	6337	—	6331	—	6343
	A'	z	—	6354	6327	6346	6327	6339
	A''	x, y	6387	6380	6377	6366	6372	6370
	A'	z	6431	6418	6422	6421	6422	6417
	A''	x, y	6481	6490	6458	6467	6452	6465
	A''	x, y	6555	6550	—	6518	6531	6524
	A'	z	—	6553	6530	6521	—	6493
$^3F_4$	A''		—	6801	—	6776	—	6783
	A''		—	6831	—	6789	—	6794

Table 1. (Continued.)

			NBW		NBMo		LBMo	
$^{2S+1}L_J$	IR	$\|\|$	E_o	E_c	E_o	E_c	E_o	E_c
	A'	z	6 848	6 837	—	6 800	—	6 805
	A'	z	—	6 857	6 824	6 826	6 832	6 834
	A'		—	7 002	—	6 957	—	6 982
	A''	x, y	—	7 009	6 970	6 970	6 992	6 989
	A''	x, y	7 021	7 021	6 997	6 999	—	7 011
	A'		—	7 023	—	6 986	—	7 002
	A'	z	7 097	7 109	7 065	7 067	7 070	7 077
$^1G_4$	A''		—	9 600	—	9 643	—	9 639
	A'	z	—	9 619	9 650	9 646	9 679	9 671
	A''	x, y	—	9 763	9 734	9 733	9 735	9 740
	A'		—	9 792	—	9 771	—	9 780
	A'		—	9 966	—	9 933	—	9 982
	A''		—	10 009	—	9 980	—	9 993
	A'		—	10 116	—	10 093	—	10 138
	A''		—	10 137	—	10 154	—	10 194
	A'		—	10 456	—	10 396	—	10 361
$^1D_2$	A'	z	16 583	16 581	16 550	16 553	16 526	16 532
	A'	z	16 623	16 626	16 581	16 590	16 569	16 572
	A''	x, y	16 840	16 831	16 794	16 778	16 778	16 767
	A''	x, y	16 866	16 874	—	16 852	16 803	16 806
	A'		—	17 103	—	17 056	—	17 059
$^3P_0$	A'	z	20 519	20 523	20 445	20 442	20 420	20 423
$^1I_6$	A'		—	21 011	—	20 940	—	20 911
$^1I_6$	A'	z	—	21 018	20 950	20 949	20 935	20 930
$^3P_1$	A''	x, y	21 073	21 070	20 987	20 981	20 968	20 965
$^3P_1$	A''		—	21 079	—	20 999	—	20 970
$^3P_1$	A'		—	21 194	—	21 108	—	21 102
$^1I_6$	A''	x, y	—	21 209	21 116	21 132	—	21 134
$^1I_6$	A'	z	—	21 226	21 159	21 146	—	21 147
$^1I_6$	A''	x, y	21 263	21 258	21 195	21 187	—	21 146
$^1I_6$	A'		—	21 282	—	21 216	—	21 192
$^1I_6$	A''	x, y	—	21 440	21 391	21 391	—	21 324
$^1I_6$	A''	x, y	21 486	21 491	—	21 397	21 375	21 372
$^1I_6$	A'		—	21 601	—	21 521	—	21 480
$^1I_6$	A''	x, y	21 783	21 784	—	21 709	21 699	21 707
$^1I_6$	A'	x, y	—	21 787	21 702	21 710	—	21 708
$^1I_6$	A'	z	—	21 837	21 763	21 767	—	21 744
$^1I_6$	A''		—	21 840	—	21 758	—	21 746
$^3P_2$	A'	z	22 198	22 193	22 100	22 104	22 091	22 089
	A''	x, y	22 293	22 296	22 203	22 208	22 186	22 187
	A'		—	22 319	—	22 222	—	22 223
	A''		—	22 319	—	22 229	—	22 191
	A'		—	22 403	—	22 321	—	22 316
$^1S_0$	A'		—	46 230	—	46 125	—	46 200

scarcity of observed Pr^{3+} transitions would be an indication of higher S_4 symmetry. However, a careful scrutiny of the $^1D_2$ splitting clearly reveals the existence of four transitions for NBW

and three for NBMo and LBMo, i.e. more transitions than the two that could be observed from the ground $^3H_4$ Stark level for a S_4 environment (since the GSA of $^3P_0$ is observed in a π-spectrum, the IR of the ground $^3H_4$ Stark level would be Γ_2, and only two $^3H_4(0) \rightarrow {}^1D_2$ transitions, one to a Γ_1 level, in the π-spectrum, and another to a $\Gamma_{3,4}$ one, in the α, σ-spectrum, would be allowed). Consequently, the assignment of the observed transitions has been carried out considering a C_2 symmetry crystal field potential around Pr^{3+} centres.

4.2.2. Crystal field analysis. In analysing the energy level structure of Pr^{3+} in NBW, NBMo and LBMo crystals for C_2 symmetry, the free-ion and crystal field, CF, Hamiltonian matrices for the entire $4f^2$ configuration were diagonalized simultaneously. In this manner, all intermediate coupling and CF J-mixing effects are included in calculations. The free-ion Hamiltonian is expressed by [18]

$$H_{\mathrm{FI}} = H_0 + \sum_{k=0,1,2,3} E^k e_k + \zeta_{4\mathrm{f}} A_{\mathrm{SO}} + \alpha L(L+1) + \beta G(G_2) + \gamma G(R_7) + \sum_{k=0,2,4} M^k m_k + \sum_{i=2,4,6} P^i p_i. \quad (1)$$

The predominant terms in this Hamiltonian are the electrostatic and spin–orbit interactions represented by E^k and ζ parameters. The remaining terms represent smaller interactions, which nevertheless play an important role in the accurate description of the energy level structure of Pr^{3+}. These are the configuration interactions (α, β, γ) and spin–spin and spin–other-orbit interactions, represented by parameters M^k, and the two-body electrostatically correlated magnetic interactions, with parameters P^k.

The one-electron CF Hamiltonian is expressed as

$$H_{\mathrm{CF}} = \sum_{k,q} B^k_q C^{(k)}_q \quad (2)$$

where $k = 2, 4, 6$ (with $|q| \leqslant k$), $C^{(k)}_q$ are the intraconfigurational Racah spherical tensors of rank k and order q [19] and the B^k_q represent one-electron CF splitting parameters with $B^k_{-q} = (-1)^q B^k_q$.

Though the above described one-electron CF approximation is usually efficient for most rare earth compounds, generally it does not describe the experimental Pr^{3+} energy level diagrams with enough accuracy. To improve the theoretical description, two-electron CF interactions (correlated CF) have been considered through spin and orbitally correlated CF models [20–24] but this seems to have met with little success. Some improvements have been reported considering interconfigurational interactions—first in the free-ion [25] and in the CF Hamiltonians, including now odd-rank CF parameters, through third-order perturbation terms [26, 27]. The experimental uncertainty imposed by the broad bands observed for Pr^{3+} in the title disordered hosts compel the current fit to be restricted to the one-electron part of the CF Hamiltonian, equation (2).

For Pr^{3+} in C_2 symmetry, 14 independent CF parameters must be adjusted to give the best overall agreement between the calculated and observed Stark levels, which are characterized by one-dimensional IR corresponding to the C_2 point group, $A' \equiv \Gamma_1$ or $A'' \equiv \Gamma_2$. The procedure followed in the fitting process is parallel to that previously described and successfully used for Pr^{3+} in $KGd(WO_4)_2$ single crystals [28]. As starting values for free-ion parameters we used the classical ones from the literature [18]. Some constraints have been imposed in order to reduce their number in the fit. The β values (for Na hosts) and M^k and P^k integrals were held constant after some tests to determine reasonable magnitudes for them. The magnitude of γ, which depends critically on the position of the $^1S_0$ state, was also fixed to a customary value,

Table 2. Free-ion and CF parameters (cm^{-1}) for Pr^{3+} in $MBi(XO_4)_2$, M = Na, Li and X = W, Mo, single crystals. Values in parentheses refer to estimated standard deviations of the indicated parameters. Values in square brackets were not allowed to vary in the parameter fitting.

	NBW	NBMo	LBMo
E^0	9589(2)	9562(2)	9566(2)
E^1	4517(2)	4504(2)	4511(2)
E^2	21.56(2)	21.55(2)	21.42(2)
E^3	457.8(1)	456.5(1)	456.2(1)
α	20.48(7)	20.13(9)	19.87(7)
β	[−501]	[−532]	−547(7)
γ	[1470]	[1470]	[1470]
ζ	736(1)	743(1)	741(1)
$M^{0,\,a}$	[2.00]	[2.75]	[2.50]
$P^{2,\,b}$	[30]	[50]	[30]
B_0^2	363(13)	358(9)	402(10)
B_2^2	27(10)	46(7)	7(12)
B_0^4	−1018(30)	−999(25)	−869(24)
B_2^4	−31(29)	−63(31)	−8(30)
S_2^4	−37(29)	110(36)	68(30)
B_4^4	−670(29)	−681(22)	−563(32)
S_4^4	−892(25)	−893(36)	[−995]
B_0^6	−321(56)	−132(50)	−300(44)
B_2^6	231(57)	214(63)	317(42)
S_2^6	−127(45)	−167(41)	−162(37)
B_4^6	−1085(42)	−936(36)	−760(37)
S_4^6	−220(48)	−195(48)	−255(44)
B_6^6	−484(57)	−461(36)	−505(32)
S_6^6	253(55)	−33(62)	−227(68)
l	32	39	36
d_m	8.1	9.7	8.1
σ^c	12.6	13.6	12.1
Residue	2075.3	3706.2	2346.1

[a] M^0, M^2, M^4 were constrained by the ratios $M^2 = 0.56M^0$, $M^4 = 0.32M^0$.
[b] P^2, P^4, P^6 were constrained by the ratios $P^4 = 0.75P^2$, $P^6 = 0.50P^2$.
[c] $\sigma = \left[\sum(\Delta_i)^2/(l-p)\right]^{1/2}$, $\Delta_i = E_o - E_c$; l: number of levels; p: number of parameters.

1470 cm^{-1}. The remaining free-ion and CF parameters were allowed to vary freely in final adjustment cycles.

Taken into account the similarity with the crystallographic situation for Nd^{3+} in NBW single crystals, as inferred from the similarity in size of Pr^{3+} and Nd^{3+} cations, the set of CF parameters calculated for the $4f^3$ configuration [16] have been used as starting values in the current analyses. The IMAGE routine [29] was used to perform the present CF analysis. In spite of the modest number of observed Stark levels, the simulation reproduces very adequately the Pr^{3+} NBW, NBMo and LBMo level sequences, with overall agreements of $\sigma = 12.6$, 13.6 and 12.1 cm^{-1}, respectively. This uncertainty is small considering the experimental precision inherent to large linewidths. The calculated energies of the Pr^{3+} levels arising from the refinements are summarized in table 1, and the free-ion and CF parameters of these refinements are given in table 2.

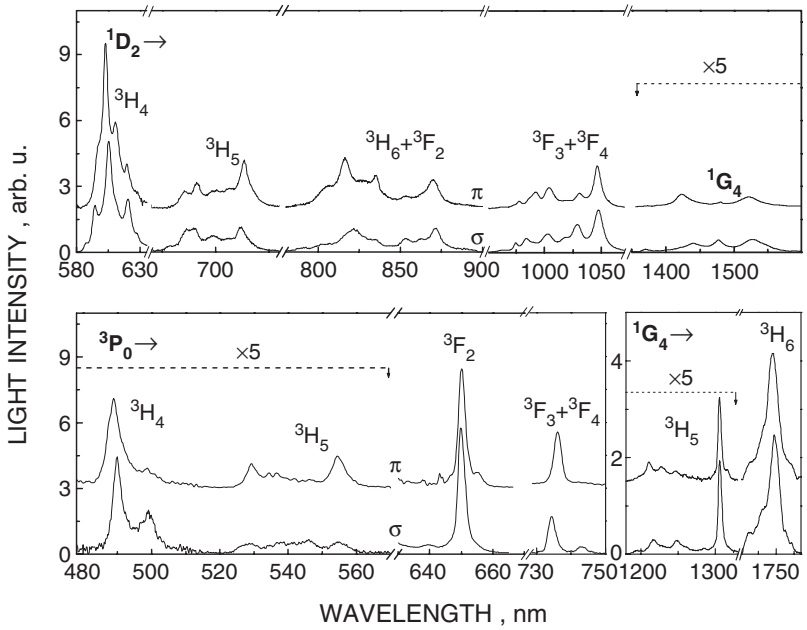

Figure 6. The 300 K polarized photoluminescence of Pr^{3+} doped NBMo excited at $^3P_2$ ($\lambda_{exc} = 454$ nm). The emissions are corrected for the equipment spectral response.

4.3. Fluorescence dynamics

4.3.1. Thermal evolution of the PL. Figure 6 shows an overview of the 300 K polarized PL of Pr^{3+} in NBMo obtained under excitation of the $^3P_2$ multiplet ($\lambda = 454$ nm). Similar results found for NBW and LBMo are not shown for the sake of brevity. The emissions observed at room temperature arise from the de-excitation of the $^3P_0$, $^1D_2$ and $^1G_4$ multiplets. These results allow us to determine their experimental emission branching ratios, β.

Figure 7(a) shows the thermal evolution of the Pr^{3+} $^3P_0 \rightarrow {}^3F_2$ and $^1D_2 \rightarrow {}^3H_4$ transitions in NBMo. Similar results, not shown for the sake of brevity, were also found for NBW. The σ-polarized $^3P_0 \rightarrow {}^3F_2$ emission ($\approx$15 300–15 450 cm^{-1}) has an asymmetric shape. This asymmetry cannot be understood as the overlapping of emission decays to the two $^3F_2$ Stark levels with the A'' IR (5077 and 5071 cm^{-1}) since the emission bandwidth (FWHM, 58 cm^{-1} at 10 K versus 68 cm^{-1} at 300 K) is much larger than the splitting of these two levels ($\approx$6 cm^{-1}). The shape of the $^3P_0 \rightarrow {}^3F_2$ emission is most probably related to the overlapped contribution of Pr^{3+} centres in the 2b and 2d sites. Apart from the slight broadening, the spectral distribution of the $^3P_0 \rightarrow {}^3F_2$ emission does not change with temperature and only a clear decrease of the integrated PL intensity with increasing temperature is observed.

A quite different evolution with increasing temperature is observed for the $^1D_2$ decay. At the lowest temperature achieved, 10 K, we observed a band at 16 073 cm^{-1} ascribed to a $^3P_0 \rightarrow {}^3H_6$ ($\Delta E = 4371$ cm^{-1}; see table 1) decay. This assignment is confirmed by the absence of this peak under excitation in the highest energy $^1D_2$ Stark level. Other peaks (16 135, 16 363, 16 496 and the shoulder at about 16 567 cm^{-1}) are ascribed to $^1D_2$ (lowest Stark level) $\rightarrow {}^3H_4$ emissions. When the temperature is raised the intensity of these bands decreases and new emission bands appear on the higher energy side. These new bands are consistent with $^1D_2$ (excited Stark levels) $\rightarrow {}^3H_4$ decays.

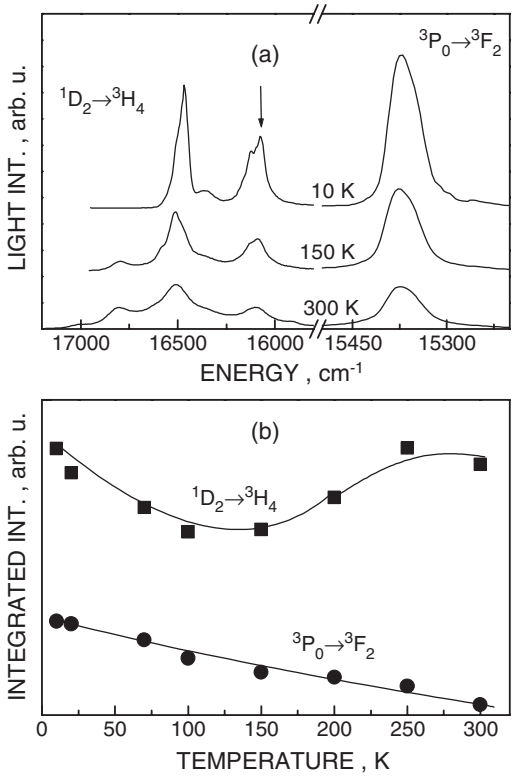

Figure 7. (a) Temperature evolution of the $^1D_2$ and $^3P_0$ σ-polarized Pr^{3+} photoluminescence in NBMo. $[Pr] = 0.6 \times 10^{20}$ cm^{-3}, $\lambda_{exc} = 488$ nm. Nominal sample temperatures are indicated for reference. The arrow shows the $^3P_0 \rightarrow {}^3H_6$ contribution. (b) The temperature dependence of the integrated emission intensity of $^1D_2$ (■) and $^3P_0$ (●) levels. The curves are a visual aid.

Figure 7(b) shows the evolution of the integrated PL intensity of the $^3P_0 \rightarrow {}^3F_2$ and ($^1D_2 \rightarrow {}^3H_4$) + ($^3P_0 \rightarrow {}^3H_6$) emissions under resonant excitation in $^3P_0$. A monotonic intensity decrease is observed for the $^3P_0 \rightarrow {}^3F_2$ emission, while the initial decrease observed for the $^1D_2$ emission is followed by an intensity recovery above 150 K. The initial intensity decrease of the $^1D_2$ emission is partially due to the contribution of the $^3P_0 \rightarrow {}^3H_6$ emission, which at 10 K contributes about 15% of the total integrated intensity.

4.3.2. Judd–Ofelt calculations. The Judd–Ofelt, JO, theory [30, 31] is widely used to calculate radiative properties of 4f transitions of rare earth ions in solid and liquid hosts. The theory uses 300 K integrated absorption cross sections such as those given in table 3 to calculate the JO parameters, Ω_k ($k = 2, 4, 6$), from which radiative transition rates, $A_{JJ'}$, luminescence branching ratios $\beta_{JJ'} = A_{JJ'}/\sum_{J'} A_{JJ'}$ and radiative lifetimes $\tau_{r,J} = 1/\sum_{J'} A_{JJ'}$ for each J manifold can be achieved.

However, it is well known that its application to Pr^{3+} suffers from some problems: the Ω_2, Ω_4 and Ω_6 values obtained depend strongly on the transitions included in the calculation; contrary to the definition, values of $\Omega_2 < 0$ are often achieved and the fits result in large deviations between calculated and experimental absorption cross sections. This is ascribed to the breaking of some of the JO theory assumptions derived from the small gap between the $4f^2$ fundamental and $4f^15d^1$ excited configuration barycentres. In order to overcome negative Ω_2

Table 3. Room temperature integrated ground state absorption cross sections, $[Pr]^{-1}\int\alpha\,\partial\lambda$, and oscillator strengths of praseodymium in $NaBi(MoO_4)_2$ crystal. $\bar{\lambda}$ is the average wavelength of the multiplet.

		$[Pr]^{-1}\int\alpha\,\partial\lambda$ (10^{-28} cm^3)		Oscillator strength $\times 10^8$		
$^{2S+1}L_J$	$\bar{\lambda}$ (nm)	σ	π	$\bar{f}_{exp}$	f_{cal}	$\lvert\Delta f_{calc}\rvert$
$^3P_2$	≈440	430	382	2305	490	1815
$^1I_6 + {}^3P_1$	≈471	449	540	2440	2111	328
$^3P_0$	≈489	178	397	1184	1485	300
$^1D_2$	≈597	146	210	526	475	52
$^1G_4$	≈1035	48	43	49	38	10
$^3F_3 + {}^3F_4$	≈1560	2738	2872	1281	1342	61
$^3F_2 + {}^3H_6$	≈1986	5500	5180	1545	1539	7

values it is customary to simply remove from the fit the $^3H_4 \rightarrow {}^3P_2$ transition [32], even setting $\Omega_2 = 0$ when it continues to result in a negative value. Anyway, this arbitrary exclusion does not solve the large uncertainties for the JO parameters obtained. Theoretical efforts beyond the JO simplifications have led to the development of oscillator strength expressions taking into account the actual energy of each excited level, including only even [33, 34] or even and odd [35–38] Ω_k parameters. Improvements of the Pr^{3+} oscillator strength fits have been found using these expressions as well as including in the fits the measured luminescence branching ratios [39], or by combined use of the two latter models [40]. Finally, a normalization of the oscillator strengths through the introduction of the uncertainty factor associated with a given experimental intensity has been used [41].

We have tested the effect of the inclusion of the $^3H_4 \rightarrow {}^3P_2$ transition and the energy dependent line strength expression developed by Kornienko [34] without finding a significant difference as regards the overall description of the experimental spectroscopic results, for both absorption and emission properties. We present here only a brief summary of the results obtained from the application of the standard JO analysis including $^3P_2$ contributions. The details of the JO treatment and definitions of the parameters can be found in previous works [28, 30, 31].

In the application of the JO theory we have taken into account the uniaxial character of the spectroscopic properties. Host refractive indices [10] and reduced matrix elements of the Pr^{3+} $J \rightarrow J'$ transitions [42] can be found in previous works. Because of the larger Pr concentration available in NBMo, the experimental uncertainty of the 300 K optical absorption determination is lower than those in NBW and LBMo; therefore we have limited the JO calculations to this host. The average oscillator strength $\bar{f}_{exp}$ values obtained were similar to those reported for Pr^{3+} in $KPr(XO_4)_2$ X = W or Mo crystals [43]. The RMS deviation was 9×10^{-6}. The JO parameters obtained for NBMo were $\Omega_2 = 9.8 \times 10^{-20}$ cm^2, $\Omega_4 = 12.8 \times 10^{-20}$ cm^2 and $\Omega_6 = 1.3 \times 10^{-20}$ cm^2. The values of Ω_6 obtained are lower than those usually found for other crystalline hosts [44]. This is due to the low intensity of the $^3H_4 \rightarrow {}^3F_3 + {}^3F_4$ transitions. In a similar way the high intensity observed for the $^3H_4 \rightarrow {}^3F_2 + {}^3H_6$ transitions leads to large Ω_2 values. These experimental facts are common to other tungstate and molybdate hosts [28, 43, 45].

The optical absorption intensities of α-spectra ($E \perp c, H \perp c$) and σ-spectra of Pr^{3+} are similar, independently of the $MBi(XO_4)_2$ lattice. This indicates that magnetic dipolar contributions to the line strengths are very weak. Nevertheless these contributions have been taken into account for transitions with $\Delta S = 0$ and $\Delta J = 0, \pm 1$. Table 4 summarizes a unique

Table 4. Total (electric dipolar, ED, and magnetic dipolar, MD) radiative transitions rates $A_{JJ'}$, calculated branching ratios $\beta_{JJ'}$ and radiative lifetimes τ_r for Pr^{3+} in NBW, NBMo or LBMo. The experimental 300 K branching ratios, β_{exp}, and 10 K lifetimes of diluted Pr samples, τ_{exp}, are given for comparison.

	λ (nm)	$A_{ED,JJ'} + A_{MD,JJ'}$ (s^{-1})	$\beta_{JJ'}$–β_{exp} (%)	$\tau_r - \tau_{exp}$ (μs)
$^3P_2$				14
$^1I_6$				70
$^3P_1$				13
$^3P_0 \rightarrow {}^1D_2$	2617.8	17	0	12–1.2
$^1G_4$	931.1	1 676	2	
$^3F_4$	734.2	9 758	12–5	
$^3F_3$	713.3	0	0	
$^3F_2$	648.5	24 403	29–68	
$^3H_6$	623.4	2 843	3–9	
$^3H_5$	554.9	0	0	
$^3H_4$	494.6	45 482	54–18	
$^1D_2 \rightarrow {}^1G_4$	1445.1	736	13–2	171–
$^3F_4$	1020.4	2 219	37	NBW: 52
$^3F_3$	980.4	258	4–10	LBMo: 36
$^3F_2$	862.1	902	15	
$^3H_6$	818.3	722	12–10	
$^3H_5$	704.2	39	1–5	
$^3H_4$	609.8	969	18–73	
$^1G_4 \rightarrow {}^3F_4$	3472.2	21	4	1 915
$^3F_3$	3048.8	2	0	
$^3F_2$	2136.8	5	1	
$^3H_6$	1886.8	202	39	
$^3H_5$	1373.6	263	50	
$^3H_4$	1054.9	28	5	
$^3F_4$				2 294
$^3F_3$				1 102
$^3F_2$				1 862
$^3H_6$				42 123
$^3H_5$				65 789

collection of radiative transition rates calculated for Pr^{3+} levels with energies equal to or lower than that of the $^3P_2$ multiplet.

The match of calculated branching ratios $\beta_{JJ'}$ with experimental ones, β_{exp}, is generally poor. This is commonly found in the JO analysis of Pr^{3+} [32] and it shows the limited value of JO treatment of Pr^{3+} transitions; therefore the radiative lifetimes can only be used as a rough reference and do not allow an accurate estimation of the non-radiative probabilities.

4.3.3. Lifetime measurements. Figure 8 shows the photoluminescence intensity decays of the $^1D_2$ level in samples with low Pr concentration, namely NBW, [Pr] $= 0.05 \times 10^{20}$ cm^{-3}, and LBMo, [Pr] $= 0.028 \times 10^{20}$ cm^{-3}. Such a low Pr concentration was not available in NBMo. These measurements were made by resonant excitation to the $^1D_2$ level ($\lambda_{exc} \approx 591$ nm) or by exciting the $^3P_0$ level ($\lambda_{exc} = 485$ nm), and detected at several emission wavelengths ($\lambda_{emi} = 605$, 620 and 712 nm). The results do not depend on the procedure used, as the radiative lifetime of the $^3P_0$ level is expected to be one order of magnitude shorter than that corresponding to the $^1D_2$ level; see table 4.

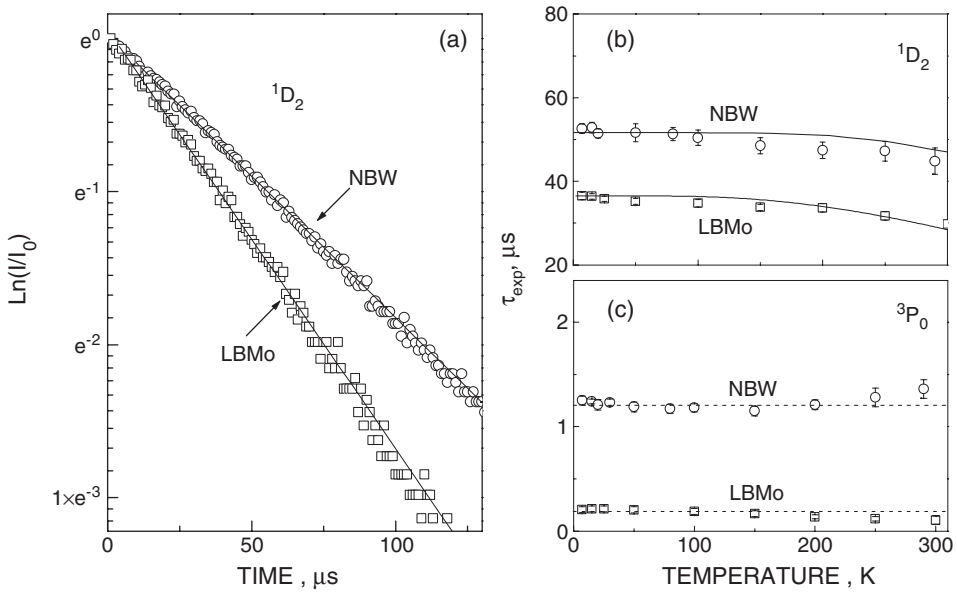

Figure 8. (a) 10 K light intensity decays of the $^1D_2$ Pr^{3+} photoluminescence in lightly doped NBW ([Pr] $= 0.05 \times 10^{20}$ cm^{-3}) and LBMo ([Pr] $= 0.028 \times 10^{20}$ cm^{-3}) samples. The points represent the experimental results and the straight lines the exponential fits. (b) The temperature dependence of the $^1D_2$ lifetime ($\lambda_{exc} = 591$ nm, $\lambda_{emi} = 605$ nm). The lines are the multiphonon relaxation fits, (ph $= 7$) $\times$ ($\hbar\varpi = 912$ cm^{-1}) for NBW and (ph $= 6.4$) $\times$ ($\hbar\varpi = 908$ cm^{-1}) + (ph $= 1$) $\times$ ($\hbar\varpi =$ 389 cm^{-1}) for LBMo. (c) The temperature dependence of the $^3P_0$ lifetime ($\lambda_{exc} = 488$ nm, $\lambda_{emi} = 650$ nm). The lines are a visual aid.

In samples with low Pr concentration the observed $^1D_2$ decays follow an exponential law providing the experimental lifetime of this level at 10 K as $\tau_{exp} = 52$ μs in NBW and $\tau_{exp} = 36$ μs in LBMo. These values are rather similar to those observed for other double tungstate or double molybdate crystals, i.e. $KGd(WO_4)_2$:0.1% Pr^{3+} ($\tau_{exp} = 40.7$ μs) [28] and $KLa(MoO_4)_2$:0.005Pr ($\tau_{exp} = 38$ μs) [45].

The experimental lifetimes decrease with increasing temperature (see figure 8(b)) and increasing Pr concentration. The $^1D_2$ decays of samples with [Pr] $> 0.05 \times 10^{20}$ cm^{-3} clearly show deviations from a single-exponential behaviour even at 10 K. Figure 9 shows the 300 K decays for NBW, NBMo and LBMo. It is clear that molybdate crystals have faster decays than tungstate lattices.

Regarding the emission decay of the $^3P_0$ level, at the lowest Pr concentrations in NBW and LBMo the decays follow a single-exponential law at all temperatures in the 7–300 K range. The experimental lifetimes found are rather insensitive to temperature and are about $\tau(^3P_0)_{exp} = 1.2$ and 0.2 μs for NBW and LBMo respectively. This temperature independence is also observed in more concentrated samples, although the lifetime decreases drastically with increasing Pr concentration and perhaps several exponential decays could contribute.

5. Discussion

First we must note the actual linewidth broadening of Pr^{3+} transitions in NBW, NBMo and LBMo. Figure 10 shows a comparison with $KGd(WO_4)_2$ ordered double tungstate. The FWHM of the $^3H_4 \rightarrow {}^3P_0$ GSA band in NBW, NBMo and LBMo are 48, 35 and 45 cm^{-1} respectively. These values are clearly larger than the 11 cm^{-1} observed for $KGd(WO_4)_2$ [28],

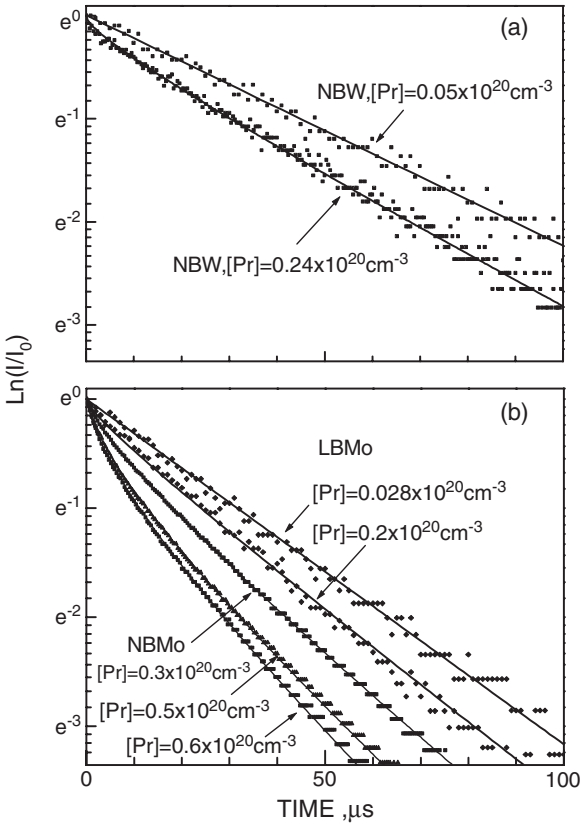

Figure 9. The concentration dependence of the $^1D_2$ 300 K experimental lifetime. (a) NBW, (b) NBMo and LBMo. The points are the experimental results and the lines the fits either to exponential laws ([Pr] $< 0.05 \times 10^{20}$ cm^{-3}) or to the Inokuti–Hirayama model, equation (6) ([Pr] $> 0.05 \times 10^{20}$ cm^{-3}).

but much smaller than the 120 cm^{-1} seen for congruent $LiNbO_3$:Pr single crystal. Therefore the broadening of Pr^{3+} bands in the $M^+Bi(XO_4)_2$ crystals considered is intermediate between those for ordered lattices and those for hosts containing defects, such as $LiNbO_3$.

It is interesting to note that for the same transition the reported 4 K linewidths of the ordered $KLa_{1-x}Pr_x(XO_4)_2$ crystals are 58 cm^{-1} for X = W and 55–75 cm^{-1} for X = Mo [43]. This difference with regard to $KGd(WO_4)_2$:Pr must be ascribed to different crystalline qualities or measurement spectral resolutions rather than to an order/disorder effect.

The broadening in $M^+Bi(XO_4)_2$ crystals must be understood as induced by the coexistence of several Pr environments around each of the two possible lattice sites, 2b and 2d. The detailed structures of these environments and the importance of their contributions to the band shape are not yet well known but the present data show that differences cannot be large. For instance, a single band, although broadened, is observed for the 10 K $^3H_4 \rightarrow {}^3P_0$ absorption transition. Moreover, the polarization features shown in figures 3–5 indicate that the optical axes of all Pr centres must be close to the lattice *c*-axis. Therefore, within the spectral resolution of our measurements the assumption of an average Pr^{3+} centre for discussing the observed spectroscopic characteristics seems a good first approach. This centre has a C_2 local symmetry lower than the S_4 one expected from the Bi^{3+} lattice sites; therefore a distortion must exist.

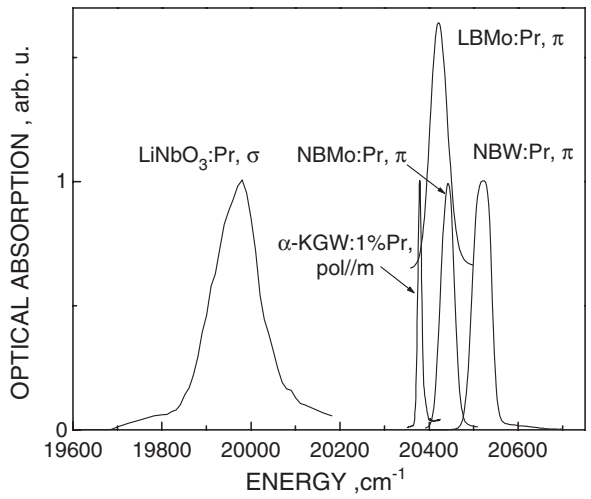

Figure 10. Comparison of the 10 K $^3H_4 \rightarrow {}^3P_0$ Pr^{3+} optical absorption line shapes for ordered, $KGd(WO_4)_2$, disordered (NBW, NBMo, LBMo) and Li-deficient, congruent $LiNbO_3$, crystal hosts.

The results of table 2 show that this distortion is quantitatively of small importance; i.e. the CF parameters involved in the distortion are small, even negligible—mainly the B_2^k ($k = 2, 4$), which are especially related to the close range coordination around Pr^{3+}.

Let us now examine the fluorescence dynamics of the $^1D_2$ multiplet potentially responsible for the stimulated emission. The experimental branching ratios obtained (see figure 6 and table 4) show that most of its optical relaxation goes to the ground $^3H_4$ multiplet to the detriment of the $^1D_2 \rightarrow {}^3F_3 + {}^3F_4$ emissions. However, similar experimental branching ratios have been found by us for Pr^{3+} in $KGd(WO_4)_2$ where stimulated emissions from this level have been achieved [4].

With the present data we can perform a first estimation of the emission cross sections, σ_{EMI}, for the $^1D_2 \rightarrow {}^3F_J$ ($J = 3, 4$) transitions and calculate the importance of the $^1G_4 \rightarrow {}^3H_4$ contribution to the photoluminescence observed in the 9000–10 500 cm^{-1} spectral region. The emission cross section of the $^1D_2 \rightarrow {}^3H_4$ transition can be calculated by the reciprocity principle [46] using the ground state absorption cross section, $\sigma_{GSA} = \alpha_{GSA}/[Pr]$:

$$\sigma_{EMI} = \sigma_{GSA} \frac{Z_l}{Z_u} e^{(E_{zl} - h\nu)/k_B T} \tag{3}$$

where Z_u and Z_l are the partition functions of the upper and lower multiplets, respectively, and E_{zl} is the energy difference between the lowest Stark levels of the two multiplets.

Figure 11(a) shows the comparison between calculated and experimental $^1D_2 \rightarrow {}^3H_4$ emission cross sections at room temperature for σ- and π-polarized configurations. Apart from the disagreement at long wavelengths due to the spectral noise and background correction, the shapes for the experimental and calculated values agree very well. Now the $^1D_2 \rightarrow {}^3F_J$ ($J = 3, 4$) emission cross sections can be obtained by the Füchtbauer–Ladenburg method [47]:

$$\sigma_{EMI} = \sigma_{EMI}^{REF} \frac{I\lambda^5}{I_{REF}\lambda_{REF}^5} \tag{4}$$

where σ_{EMI}^{REF}, I_{REF} and λ_{REF} are taken from the $^1D_2 \rightarrow {}^3H_4$ transition. Figure 11(b) shows the results obtained. A peak $^1D_2 \rightarrow {}^3F_4 + {}^3F_3$ $\sigma_{EMI} = 2.3 \times 10^{-20}$ cm^2 occurs in π polarization at $\lambda = 1046.5$ nm. These results are compared to the $^1G_4 \rightarrow {}^3H_4$ emission cross sections

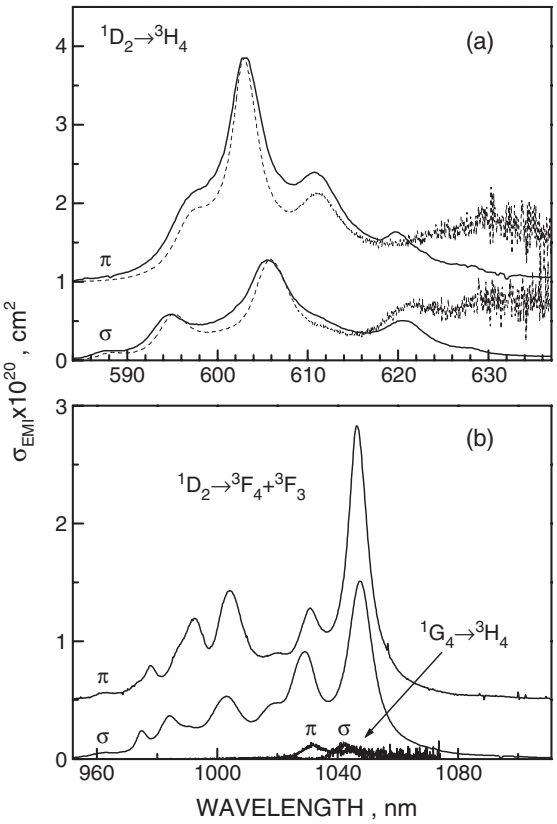

Figure 11. (a) Comparison of the experimental (continuous curves) and calculated (dashed curves) 300 K emission cross sections of the $^1D_2 \rightarrow {}^3H_4$ transition. (b) Calculated 300 K emission cross sections of the $^1D_2 \rightarrow {}^3F_4 + {}^3F_3$ and $^1G_4 \rightarrow {}^3H_4$ transitions of Pr^{3+} in NBMo.

calculated by the reciprocity principle. It is clear than the latter is negligible in comparison to the cross sections obtained for $^1D_2 \rightarrow {}^3F_J$ ($J = 3, 4$) transitions. Therefore, the $^1G_4 \rightarrow {}^3H_4$ experimental PL spectrum cannot be obtained separately and not further calculations of the $^1G_4 \rightarrow {}^3H_5$ emission cross section can be made by this method.

The low confidence in the JO analysis inherent to praseodymium prevents the comparison of radiative and experimental Pr^{3+} lifetimes in $M^+Bi(XO_4)_2$ crystals. Apart from the fact that lithium and sodium bismuth molybdates show similar Pr^{3+} $^1D_2$ lifetimes, lower than those of tungstates, in all these matrices the lifetimes decrease with increasing temperature and Pr concentration. Therefore energy transfer and multiphonon emission contribute to reduction of the population of excited levels.

These non-radiative processes are described by the characteristic multiphonon relaxation rate, τ_{ph}^{-1}, and energy transfer rate, τ_C^{-1}, which are related to the experimental, τ_{exp}^{-1}, and radiative, τ_r^{-1}, rates as $\tau_{exp}^{-1} = \tau_r^{-1} + \tau_{ph}^{-1} + \tau_C^{-1}$. The temperature dependence of the multiphonon relaxation rate is given by [48]

$$\tau_{ph}^{-1}(T) = \tau_{ph}^{-1}(0)\,(1+n)^{ph} \tag{5}$$

where $n = \left[\exp(\hbar\varpi/kT) - 1\right]^{-1}$, $\hbar\varpi$ being the energy of the phonon emitted (often taken as the cutting frequency in the Raman or infrared spectra), k the Boltzmann constant and ph the

number of phonons required to maintain the energy conservation in a non-radiative transition between the levels separated by ΔE.

Figure 8(b) showed the thermal evolution of the $^1D_2$ Pr^{3+} lifetime in NBW and LBMo. The Pr concentrations considered are low and, due to the single-exponential character of the decays, energy transfer between Pr ions can be neglected. The energy difference between the $^1D_2$ and the low lying $^1G_4$ levels can be obtained from table 1 for NBW, $\Delta E \approx 6100\ cm^{-1}$, and LBMo, $\Delta E \approx 6200\ cm^{-1}$. Assuming that the phonon emitted is the most energetic in the Raman spectrum, namely at 912 cm^{-1} for NBW and 909 cm^{-1} for LBMo [2], the number of emitted phonons to match the $^1D_2 - ^1G_4$ gap is ph ≈ 7. Figure 8(b) also shows the good fit of the experimental lifetime dependence obtained using equation (5).

The time decays of the $^1D_2$ multiplet emissions become faster with increasing Pr concentration (see figure 9), suggesting the presence of cross-pair transfer processes. The non-exponential character of the decays for high Pr concentration can be described using the continuum model developed by Inokuti and Hirayama [49]. This model assumes energy transfer from an excited Pr^{3+} donor to the continuously distributed surrounding Pr^{3+} ions in the ground state. The light intensity decay follows the law

$$I(t) = I(0)\exp\left[\frac{-t}{\tau_0} - \Gamma\left(1 - \frac{3}{s}\right)\frac{[\mathrm{Pr}]}{c_0}\left(\frac{t}{\tau_0}\right)^{3/s}\right] \tag{6}$$

where $c_0 = 3/4\pi R_c^3$ is a critical concentration related to the distance R_c at which the donor-trap energy transfer rate equals the spontaneous decay rate. $\Gamma(x)$ is the gamma function and $s = 6$, 8 and 10 correspond to electric dipole–dipole, dipole–quadrupole and quadrupole–quadrupole transfer mechanisms respectively. τ_0 is the lifetime in the absence of energy transfer.

The character of the transfer mechanism can be deduced by plotting $\ln[I(t)/I(0)] + t/\tau_0$ versus $t^{3/s}$ and using the experimental value obtained for the lowest Pr concentration as τ_0. This value was obtained as $\tau_{exp}(300\ K) = 45\ \mu s$ in NBW (see figure 9(a)). Figure 12(a) shows these representations for the NBW sample with $[Pr] = 0.24 \times 10^{20}\ cm^{-3}$. A straight line is only obtained for $s = 6$, corresponding to an electric dipole–dipole transfer.

In the case of NBMo a τ_0(300 K) value at low Pr concentration was not available and the attempt to use the value obtained for NBW leads to poor linear fitting independently of s (see figure 12(b), dashed curve). Therefore we used τ_0 as an additional free parameter in this case. For all available Pr concentrations linear fits were obtained for $s = 6$ when $\tau_0(300\ K) = 36\ \mu s$ was used; see the continuous lines of figure 12(b). This τ_0 value is close to that achieved for the lightly Pr doped LBMo sample.

Figure 12(b) also shows the fits for the RT experimental decays of the $^1D_2$ level using equation (6) with $s = 6$ and the corresponding praseodymium concentration. From these fits we have calculated the critical distance for each Pr concentration, obtaining the result $R_c \approx 1.35 \pm 0.05$ nm. This value is compared in table 5 with the average Pr–Pr distances $\bar{r} = (4\pi[\mathrm{Pr}]/3)^{-1/3}$ for each matrix. It is now clear that the Pr–Pr distance in all samples showing non-exponential decay behaviour approaches the critical distance for efficient energy transfer between $^1D_2$ levels.

The emission dynamics of the $^3P_0$ multiplet, in particular the $^3P_0/^1D_2$ radiative yield ratio, depends strongly on the crystal field strength and on the covalency of the lattice [50]. The results obtained for NBW and NBMo are similar to that observed for $Na_5La_{1-x}Pr_x(MoO_4)_4$ [50]. From figure 7 it is clear that the temperature increase depopulates the $^3P_0$ level and feeds the $^1D_2$ one. This non-radiative decay occurs most probably via the intersystem crossing of the 4f5d state. The multiphonon emission rate is now weak and a thermal excitation of the $^3P_0$ electronic population to the closely lying $^1I_6$ multiplet with a much higher radiative lifetime, see table 4, contributes to the temperature independence of this lifetime.

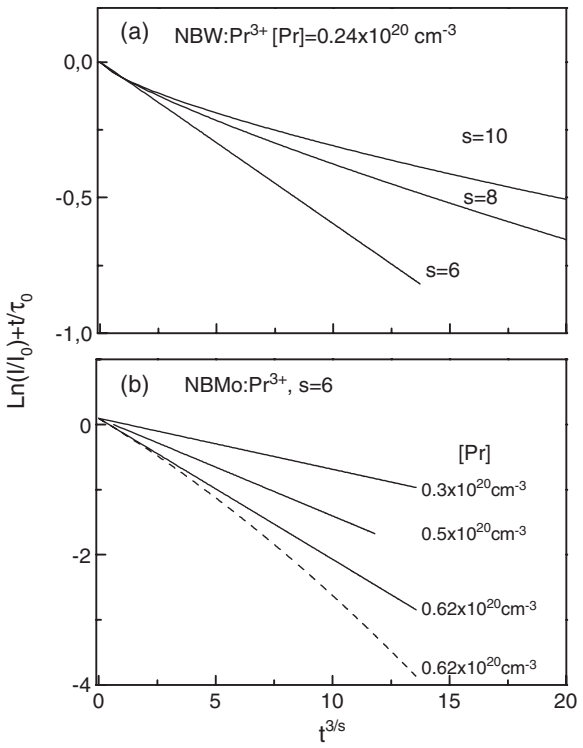

Figure 12. (a) Inokuti–Hirayama representations of the $^1D_2$ 300 K photoluminescence decay for electric dipole–dipole ($s = 6$), dipole–quadrupole ($s = 8$) and quadrupole–quadrupole ($s = 10$) transfer mechanism assumptions for NBW. $\tau_0 = 45$ μs. (b) Similar representations of the decays obtained in NBMo for increasing [Pr] assuming electric dipole–dipole transfer, $s = 6$. Straight lines are found using $\tau_0 = 36$ μs. The dashed curve corresponds to the representation if $\tau_0 = 45$ μs and $s = 6$ are assumed.

Table 5. Average Pr–Pr distances, $\bar{r}$, for different Pr concentrations and energy transfer critical distances, R_c, obtained for $MBi(XO_4)_2$ crystals.

	[Pr] (10^{20} cm^{-3})	$\bar{r}$ (nm)	R_c (nm)
NBW	0.05	3.62	
	0.24	2.15	1.31
LBMo	0.028	4.40	
	0.32	1.95	1.44
NBMo	0.3	1.91	1.33
	0.5	1.68	1.34
	0.62	1.58	1.39

6. Conclusions

It has been confirmed that the Pr^{3+} transitions in NBW, NBMo and LBMo, which are so called 'disordered crystals', show bandwidths larger than those observed in 'ordered' double tungstate or double molybdate single-crystal hosts. The 10 K bandwidths observed in NBW and LBMo are somewhat larger than that in NBMo. These large bandwidths are associated with the presence of two lattice sites for praseodymium and several environments around each site, the

latter ascribed to the M^{+}, Bi^{3+} cationic disorder. In spite of this local disorder, the different Pr centres retain well-defined relative orientations, leading to polarization rules, and exhibit a C_2 site symmetry lower than the S_4 site symmetry exhibited by the Bi^{3+} coordination polyhedra. The peak emission cross section of the $^1D_2 \rightarrow {}^3F_4 + {}^3F_3$ laser transition of Pr^{3+} in $MBi(XO_4)_2$ crystals is large and similar to that observed in double tungstate and double molybdate hosts where Pr^{3+} stimulated emissions have been achieved. For $[Pr] \geqslant 2 \times 10^{19}$ cm^{-3} the $^1D_2$ manifold partially decays non-radiatively due to an electric dipole–dipole transfer between Pr neighbours.

Acknowledgments

This work was supported by CICyT (Spain) under project MAT2002-4603-COS-S. PIXE measurements were performed within the CSIC (Spain)–GRICE (Portugal) cooperation agreement. AM is supported by CONACyT (Mexico) grant No 128118.

References

[1] Kaminskii A A, Bagayev S N, Ueda K, Nishioka H, Kubota Y, Chen X and Kholov A 1995 *Japan. J. Appl. Phys.* **34** L1461
[2] Hanuza J, Maczka M and van der Maas J H 1995 *J. Mol. Struct.* **348** 349
[3] Tzunov V K, Efremov V A and Velinkodnyi Y A 1986 *Crystallochemistry and Properties of Double Molybdates and Tungstates* (Leningrad: Nauka) (in Russian)
[4] Kaminskii A A, Bagaev S N and Pavlyuk A A 1995 *Phys. Status Solidi* a **151** K53
[5] Kaminskii A A, Li L, Butashin A V, Mironov V S, Pavyuk A A, Bagayev S N and Ueda K 1997 *Japan. J. Appl. Phys.* **36** L107
[6] Choi Y G and Heo J 1997 *J. Non-Cryst. Solids* **217** 199
[7] Volkov V, Rico M, Méndez-Blas A and Zaldo C 2002 *J. Phys. Chem. Solids* **63** 95
[8] Hanuza J, Benzar A, Haznar A, Maczka M, Pietraszko A and van der Maas J H 1996 *Vib. Spectrosc.* **12** 25
[9] Hanuza J, Haznar A, Maczka M, Pietraszko A, Lemiec A, van der Maas J H and Lutz E T G 1997 *J. Raman Spectrosc.* **28** 953
[10] Méndez-Blas A 2003 Espectroscopía óptica de lantánidos en dobles volframatos y molibdatos sin trasformación polimórfica *PhD Report* Universidad Autónoma de Madrid
[11] Volkov V and Zaldo C 1999 *J. Cryst. Growth* **206** 60
[12] Popova M N, Klimin S A, Malkin B Z, Kasatkina L A, Cao G and Crow J 1996 *Phys. Lett.* A **223** 308
[13] Etsell T H and Flengas S N 1970 *Chem. Rev.* **70** 339
[14] Pawlak D, Frukacz Z, Mierczyk Z, Suchocki A and Zachara J 1998 *J. Alloys Compounds* **275–277** 361
[15] de Mello Donegá C, Ellens A, Meijerink A and Blasse G 1993 *J. Phys. Chem. Solids* **54** 293
[16] Méndez-Blas A, Volkov V, Cascales C and Zaldo C 2001 *J. Alloys Compounds* **323/324** 315
[17] Rico M, Volkov V, Cascales C and Zaldo C 2002 *Chem. Phys.* **279** 73
[18] Carnall W T, Goodman G L, Rajnak K and Rana R S 1989 *J. Chem. Phys.* **90** 3443
[19] Wybourne B G 1965 *Spectroscopic Properties of Rare Earths* (New York: Wiley–Interscience)
[20] Judd B R 1977 *Phys. Rev. Lett.* **34** 242
[21] Judd B R 1989 *J. Phys. C: Solid State Phys.* **13** 2695
[22] Judd B R 1979 *J. Lumin.* **18/19** 604
[23] Crosswhite H and Newman D J 1984 *Phys. Status Solidi* b **126** 381
[24] Yeung Y Y and Newman D J 1987 *J. Chem. Phys.* **86** 6717
[25] Kornienko A A, Dunina E B and Yankevich V L 1995 *Opt. Spectrosc.* **79** 700
[26] Garcia D and Faucher M 1989 *J. Phys. Chem.* **91** 7461
[27] Kornienko A A, Dunina E B and Kaminskii A A 1999 *J. Exp. Theor. Phys.* **89** 1130
[28] Zaldo C, Rico M, Cascales C, Pujol M C, Massons J, Aguiló M, Díaz F and Porcher P 2000 *J. Phys.: Condens. Matter* **12** 8531
[29] Porcher P, Fortran routines REEL and IMAGE for simulation of d^N and f^N configurations involving real and complex crystal-field parameters, unpublished
[30] Judd B R 1962 *Phys. Rev.* **127** 750
[31] Ofelt G S 1962 *J. Chem. Phys.* **37** 511

[32] Bowlby B E and di Bartolo B 2002 *J. Lumin.* **100** 131
[33] Kornienko A A, Kaminskii A A and Dunina E B 1990 *Phys. Status Solidi* b **157** 261
[34] Kornienko A A, Kaminskii A A and Dunina E B 1990 *Phys. Status Solidi* b **157** 267
[35] Eyal M, Greenberg E, Reisfeld R and Spector N 1985 *Chem. Phys. Lett.* **117** 108
[36] Flórez A, Messaddeq Y, Malta O L and Aegerter M A 1995 *J. Alloys Compounds* **227** 135
[37] Auzel F, Hubert S and Delamoye P 1982 *J. Lumin.* **26** 251
[38] Flórez A, Malta O L, Messaddeq Y and Aegerter M A 1997 *J. Non-Cryst. Solids* **213/214** 315
[39] Quimby R S and Miniscalco W J 1994 *J. Appl. Phys.* **75** 613
[40] Merkle L D, Zandi B, Montcorgé R, Guyot Y, Verdun H R and McIntosh B 1996 *J. Appl. Phys.* **79** 1849
[41] Goldner P and Auzel F 1996 *J. Appl. Phys.* **89** 7972
[42] Weber M J 1968 *J. Chem. Phys.* **48** 4774
[43] Macalik L, Hanuza J, Sokolnicki J and Legendziewicz J 1999 *Spectrochim. Acta* A **55** 251
[44] Görller-Walrand C and Binnemans K 1998 *Handbook on the Physics and Chemistry of Rare Earths* vol 25, ed K A Gschneidner Jr and L Eyring (Amsterdam: Elsevier) chapter 167, p 101
[45] Macalik L, Ryba-Romanowski W, Golab S, Hanuza J and Legendziewicz J 1996 *Acta Phys. Pol.* A **90** 301
[46] McCumber D E 1964 *Phys. Rev.* **136** A954
[47] Aull B F and Jenssen H P 1982 *IEEE J. Quantum Electron.* **18** 925
[48] Riseberg L A and Moss H W 1968 *Phys. Rev.* **174** 429
[49] Inokuti M and Hirayama F 1965 *J. Chem. Phys.* **43** 1978
[50] de Mello Donegá C, Meijerink A and Blasse G 1995 *J. Phys. Chem. Solids* **56** 673